THE INFLUENCE OF HEAT TREATMENTS ON THE MICROSTRUCTURE AND TENSILE PROPERTIES OF ADDITIVELY MANUFACTURED INCONEL 939

Rukesh Gusain[1,2], Mohammad Soleimani Dodaran[1,2], Paul R. Gradl[3], Nima Shamsaei[1,2], Shuai Shao[1,2*]

[1]National Center for Additive Manufacturing Excellence (NCAME), Auburn University, Auburn, AL 36849, USA
[2]Department of Mechanical Engineering, Auburn University, Auburn, AL36849, USA
[3]NASA Marshall Space Flight Center, Propulsion Department, Huntsville, AL 35812, USA

*Corresponding author:
Email: sshao@auburn.edu
Phone: (334) 844 4867

Abstract

This study investigated the effect of heat treatment variations on the microstructure and tensile properties of laser powder bed fused Inconel 939 manufactured via laser powder bed fusion. Three different heat treatment schedules, all of which comprise stress relief, hot isostatic pressing, solution annealing, and aging, were followed, and resulting changes in microstructure were analyzed using scanning electron microscopy. Tensile tests were conducted on specimens subjected to different heat treatments to evaluate the mechanical properties at room temperature. Microstructural results showed that solution treatment at 1190 °C for 4 h led to better removal of dendritic microstructure, while second-step aging at 850 °C resulted in monomodal distribution of precipitates. However, the second-step aging temperatures from 750 to 800 °C resulted in bi-modal distribution. The optimal heat treatment schedule, which yielded a superior combination of strength and ductility, involved solution treatment at 1190 °C for 4 h and two-step aging at 1000 °C for 6 h and 800 °C for 4 h.

Keywords: Laser powder bed fusion (L-PBF), nickel base superalloy, γ' precipitate, heat treatment effects, tensile properties

Introduction

Inconel 939 (IN939) is a γ' precipitate-strengthened nickel-base superalloy, which is widely used to fabricate vanes and blades of industrial gas turbines [1–3]. The complex geometries in such applications make conventional manufacturing (CM) techniques less suitable. Additive manufacturing (AM) is becoming popular among manufacturing industries due to its ability to fabricate parts with intricate geometries in an cost effective and expedited manner [4,5]. Despite offering several benefits, AM parts in the as-fabricated condition often possess inhomogenous microstructure (i.e., elongated grains along the build direction and equiaxed grains in the plane perpendicular to the build direction) and lack strengthening precipitates, which leads to sub-optimal mechanical performance [4,6,7]. It has been observed that the primary strengthening phase of IN939, the γ' phase, does not readily form in the as-fabricated additively manufactured IN939 due to the suppression of diffusion-driven precipitation reaction because of the fast-cooling rate during the manufacturing process [7,8]. The size and morphology of γ' phase plays a crucial role in determining the mechanical response of an alloy [9]. In order to achieve desirable microstructure and precipitate size distribution, additively manufactured IN939 parts are usually heat treated.

The treatment schedule proposed during the compositional development of IN939 includes solution treatment (ST) at 1160°C for 4h and aging at 850°C for 16h [10–12]. However, due to dissimilarity in the microstructure of parts manufactured via AM and CM techniques, the heat-treatment schedule designed for CM parts may not be applicable for the AM parts. Studies on additively manufactured IN939 have reported the formation of γ' precipitates and Ti, Nb and Ta-rich MC carbides after the solution treatment [13–16]. The temperature variation and the sequence of the heat treatment steps may alter the volume fraction and distribution of these γ' phases and carbides [17,18], which in turn, may result in different mechanical properties. Hence, a heat treatment schedule should be designed appropriately before applying additively manufactured IN939 in the safety-critical applications mentioned earlier. This study aims to investigate the effect of various heat treatments on the microstructure and tensile properties of laser powder bed fused (L-PBF) IN939.

Experimental Details

IN939 bars were fabricated in an EOS M290 system using the process parameters listed in **Table 1**. The chemical composition of the powder used in this study is tabulated in **Error! Reference source not found.**. The fabricated specimens were divided into several groups and subjected to various heat treatments. A combination of different soaking times and temperatures were studied for various heat treatment steps and are designated as HT1, HT2, and HT3 in **Table 3**. The acronyms in **Table 3**: FC, WQ, and AC stand for furnace-cooled, water-quenched, and air-cooled, respectively.

The microstructural features were analyzed on the radial plane (perpendicular to the build direction (BD)) of samples using a Zeiss Crossbeam 550 scanning electron microscope (SEM) equipped with energy dispersive spectroscopy (EDS) and Electron backscatter diffraction (EBSD) detectors. For this, microstructural samples were cut from the non-heat treated (NHT) and heat treated (HT) specimens using an abrasive cutter. The excised samples were mounted, ground, and polished using sand papers with grit from 320 to 4000.

The bars were machined to final geometry for tensile testing according to ASTM E8 standard, as shown in **Figure 1**. Quasi-static tensile tests were conducted on these specimens using an MTS servo-hydraulic machine. An extensometer was attached during the tensile tests untill a 0.05 mm/mm strain. After that, the extensometer was removed from the specimen to prevent extensometer damage and the remaining test was continued under displacement controlled mode until failure.

Table 1. Process parameters used to fabricate L-PBF IN939 bars.

Power	285 W
Layer Thickness	40 µm
Speed	960 mm/s
Hatch Spacing	0.11 mm

Table 2. Chemical composition of IN939 powder used in this study.

Elements	Ni	Cr	Co	Ti	W	Al	Ta	Nb	C	Zr	B	Mo
Weight %	48.24	22.5	19	3.7	2	1.9	1.4	1	0.15	0.1	0.01	<0.01

Table 3. Details of heat treatment schedules investigated in this study.

Heat treatment schedules	**Stress relief (SR)**	**Hot isostatic pressing (HIP)**	**Solution treatment (ST)**	**Embryonic aging**	**Primary aging**	**Secondary aging**
HT1	900 °C for 4 h FC	1163 °C @ 103 MPa for 4 h FC	1160 °C for 4 h WQ	950 °C for 0.5 h FC	950 °C for 8 h WQ	750 °C for 8 h WQ
HT2	900 °C for 4 h FC		1160 °C for 4 h WQ	950 °C for 0.5 h FC	950 °C for 8 h WQ	850 °C for 8 h WQ
HT3	900 °C for 4 h FC		1190 °C for 4 h AC		1000 °C for 6 h AC	800 °C for 4 h AC

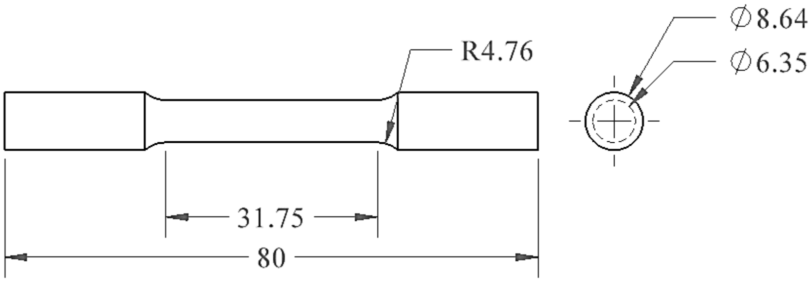

Figure 1. Tensile specimen geometry of L-PBF IN939 (All dimensions are in mm).

Results and Discussion

An inverse pole figure (IPF) map and a backscattered electron (BSE) image obtained from the radial plane of NHT L-PBF IN939 are presented in **Figure 2** (a) and (b), respectively. The average diameter of grains was 7.5 µm with a standard deviation of 8.7 µm. The statistics of grains were obtained by post processing the results EBSD scans with a step size of 0.4343 µm. The high-magnification BSE micrograph showed the presence of dendritic microstructure in the NHT sample (see **Figure 2** (b)). EDS analysis on the radial plane of the NHT sample revealed significant segregation of Ti and Nb and minor segregation of Ta and W at the inter-dendritic regions. In addition, there was a slight depletion of Ni and Co in those regions (see **Figure 3**). Additively manufactured metallic parts often possess such dendritic microstructure and segregation of alloying elements due to very high cooling rates during the manufacturing process [9,11,19].

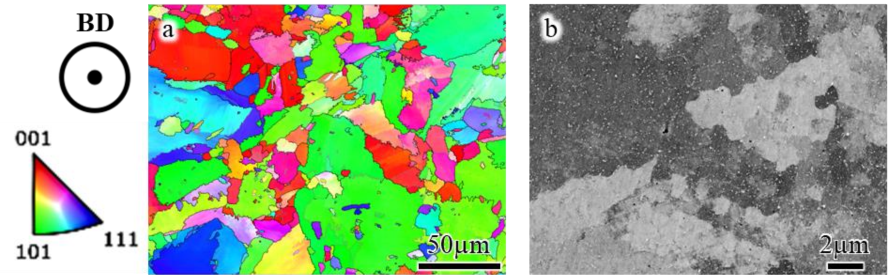

Figure 2. NHT microstructure of L-PBF IN939 in the radial plane (a) IPF map (b) BSE micrograph.

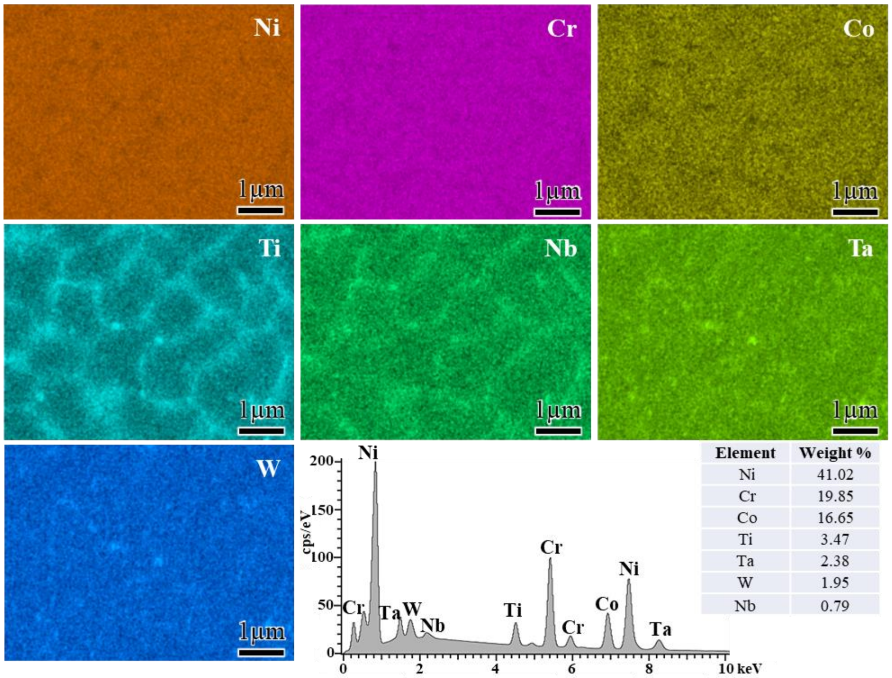

Element	Weight %
Ni	41.02
Cr	19.85
Co	16.65
Ti	3.47
Ta	2.38
W	1.95
Nb	0.79

Figure 3. Elemental maps obtained from the radial plane of NHT L-PBF IN939.

The BSE micrographs obtained from the radial planes of samples subjected to different solution treatments are shown in **Figure 4**. These BSE micrographs show that Ti, Nb, and Ta- rich MC carbides were precipitated after the solution treatment (see EDS analysis in **Figure 5**). These MC carbides can be found at the grain boundaries and within the grains. It can also be observed that solution treatment at 1190 °C for 4 h resulted in better removal of dendritic structures (see **Figure 4** (b)) compared to one solution treated at 1160 °C for 4 h.

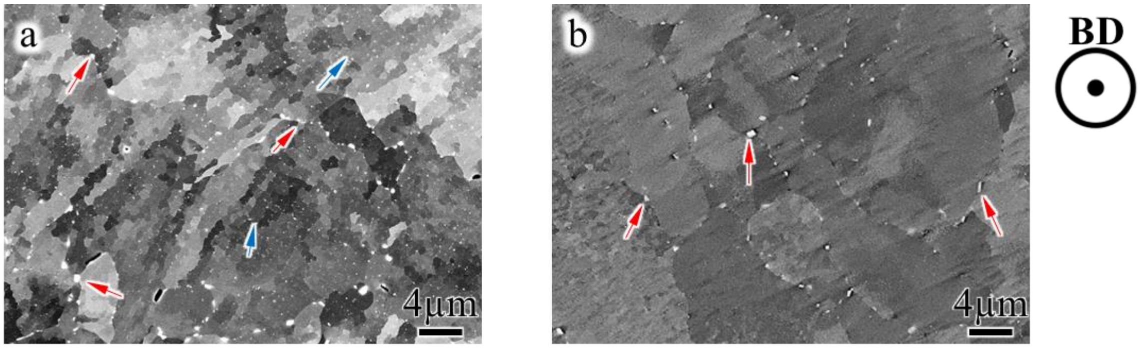

Figure 4. BSE micrographs obtained from radial planes of L-PBF IN939 subjected to solution treatments at a) 1160 °C for 4 h b) 1190 °C at 4 h. Red and blue arrowheads point to carbides at grain boundaries and within grains, respectively.

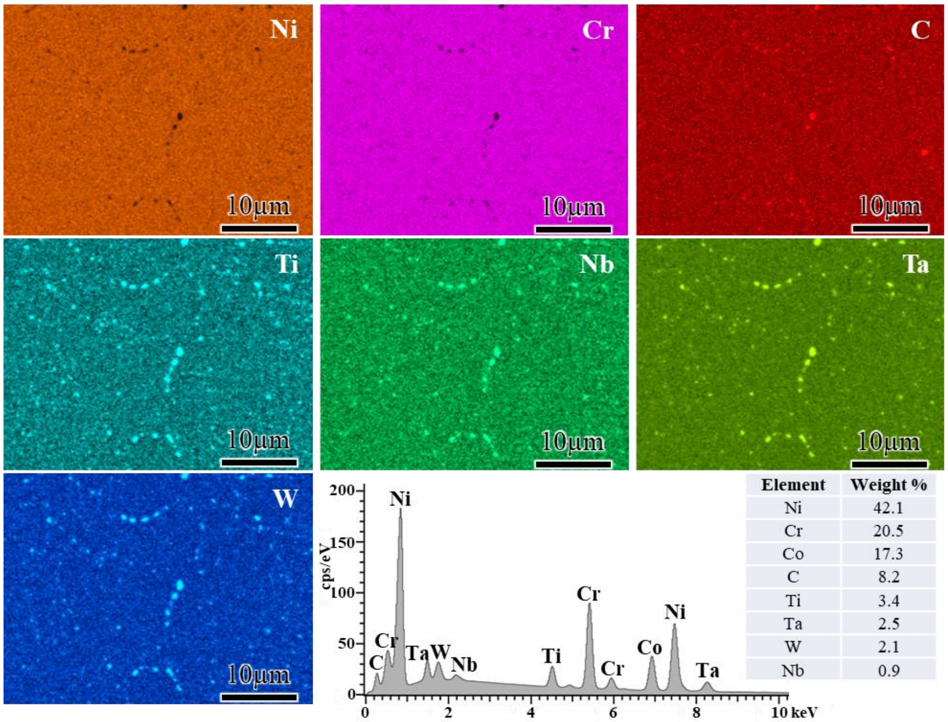

Element	Weight %
Ni	42.1
Cr	20.5
Co	17.3
C	8.2
Ti	3.4
Ta	2.5
W	2.1
Nb	0.9

Figure 5. EDS of heat treated L-PBF IN939 exhibiting local enrichment of Nb, Ta, Ti, and W.

The IPF maps and BSE micrographs for all heat treatment schedules investigated in this study are shown in **Figure 6**. The average grain sizes for all heat treatment schedules are shown at the bottom of their corresponding IPF maps. In terms of different heat treatment schedules, the grain size followed the sequence: HT1<HT2<HT3. A higher heat treatment temperature resulted in a slightly larger grain size. This can be ascribed to the better dissolution of carbides along the grain boundaries at higher temperatures, thereby removing their pinning effect [11].

The dendritic microstructure present after the solution treatment step further dissolved during the later heat treatment stages. It is worth mentioning that HT1 and HT3 resulted in bimodal γ' precipitates (see **Figure 6** (c) and (i)). The sizes of primary and secondary precipitates are listed in **Table 4**. Also, it can be seen that lower aging temperatures always resulted in bimodal precipitate size, even if same solution treatment is applied (HT1 and HT2). This is because, higher aging temperatures permit higher diffusion rate which promotes the growth of the γ′ precipitates . Smaller precipitates also tend to be consumed by larger ones under the Ostwald's ripening mechanism. In contrast, at lower temperatures, while the nucleation of γ′ is encouraged due to undercooling, their growth are relatively slow due to the more sluggish diffusion. These could be the reasons behind larger precipitates observed in HT2 sample when compared with HT1 ones (see **Figure 6** (c) and (f)). Moreover, HT3 specimens had the largest primary γ′ precipitates which also can be attributed to the higher solution treatment (1190 °C) and primary aging temperatures (1000 °C).

Table 4. Comparison of γ′ precipitate sizes.

	Precipitate sizes (nm)		
	HT1	HT2	HT3
Primary γ′	140	153	205
Secondary γ′	35	N/A	20

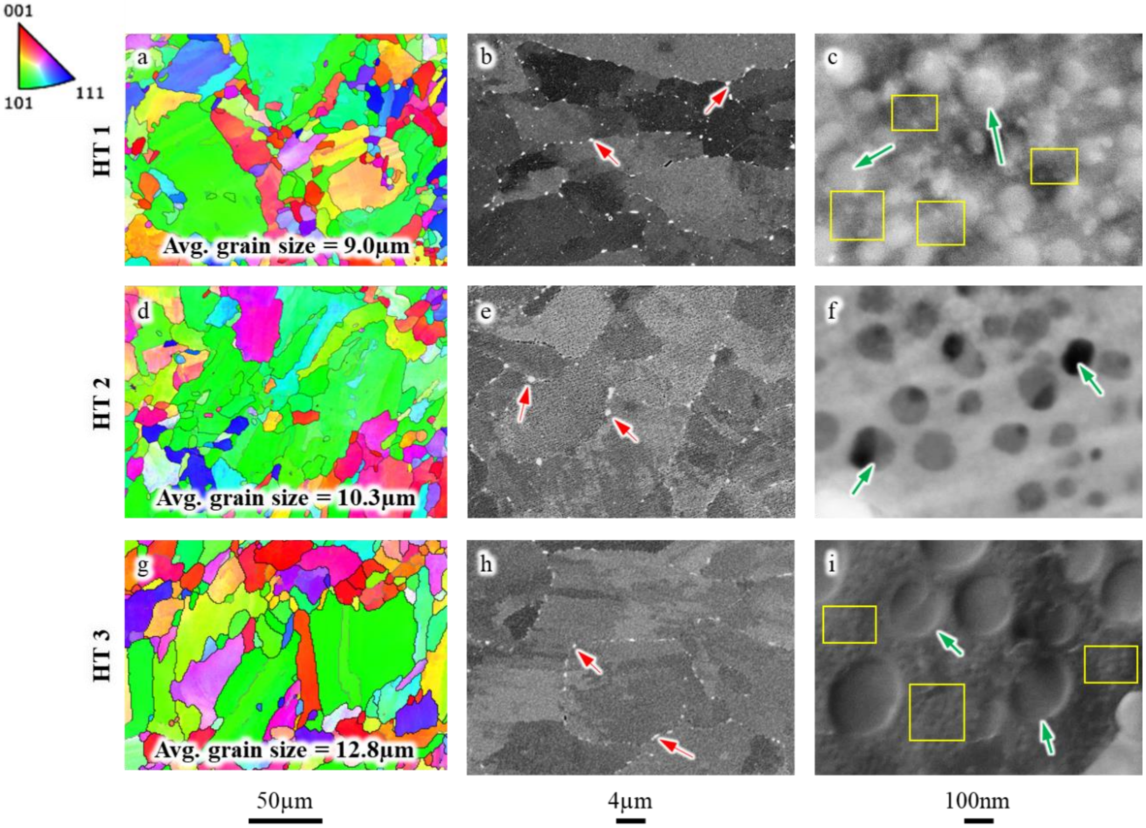

Figure 6. IPF maps and BSE micrographs obtained from radial planes of L-PBF IN939 subjected to different heat treatment schedules. (Red arrowheads point to grain boundary carbides. Green arrowheads and yellow boxes point to primary and secondary γ′ precipitates respectively.)

The engineering stress-strain curves and the variation of the ultimate tensile strength (UTS), yield strength (YS), and elongation at failure (EL) of HT L-PBF IN939 are presented in **Figure 7**. As seen in **Figure 7** (b), the YS of HT1 specimens was 12.9% greater than HT2 and 2.9% greater than HT3, whereas the elongation to failure was 2% lower than HT2 and 12% lower than HT3. The strengths of HT1 and HT3 were higher than HT2 due to the presence of secondary γ′ precipitates. These closely spaced secondary γ′ precipitates can significantly impede dislocation movement and strengthen the alloy [9,20]. Among all three specimens, HT1 resulted in higher tensile strength. This may be because of the smaller spacing between the primary γ′ precipitates in HT1 specimen (see **Figure 6** (c) and (o)).

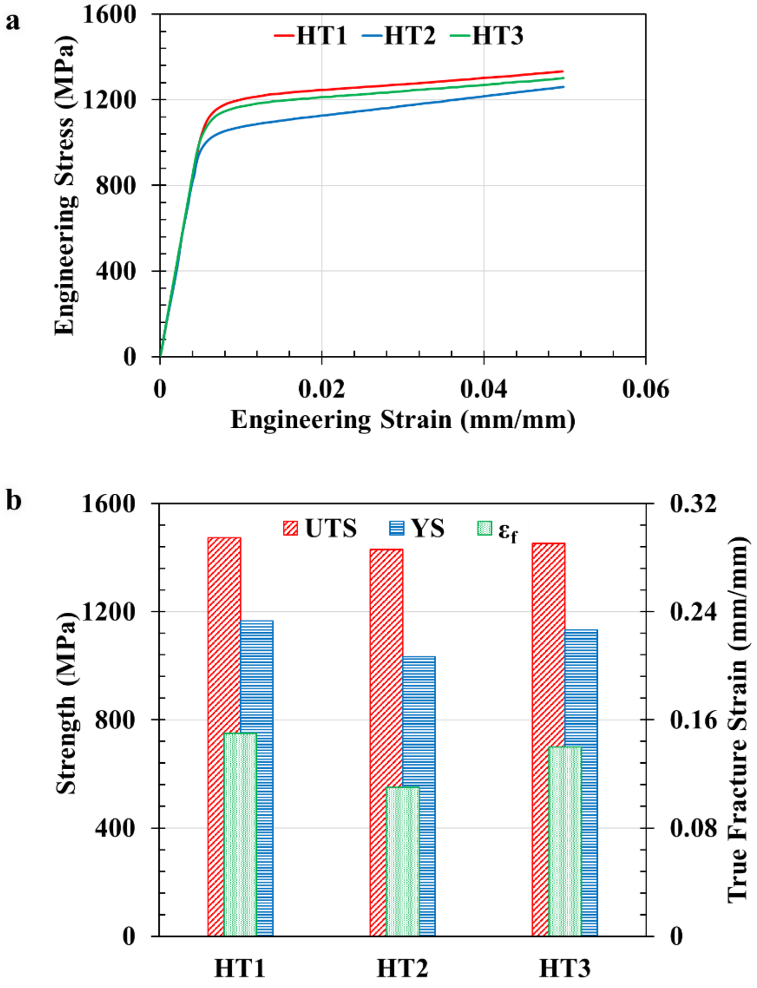

Figure 7. Tensile behavior of HT L-PBF IN939 (a) Engineering stress-strain curves (b) bar chart showing variations in tensile properties such as UTS, YS and EL.

Conclusions

In this study, the effect of heat treatments was investigated on the microstructure and mechanical properties of L-PBF IN939. The following conclusions can be drawn from the results obtained in this study.

- The non-heat treated microstructure showed presence of dendritic microstructure with significant segregation of Ti and Nb and minor segregation of Ta and W. These segregated elements partially dissolved during the solution treatment and re-precipitated as MC carbides.
- When comparing the heat treatment schedules with the same solution treatment temperature, bimodal precipitate size is resulted at lower secondary aging temperature.
- The heat treatments that resulted in bimodal precipitate size distributions provided better mechanical strength due to presence of secondary γ' precipitates which strongly impede dislocation motion. The tensile strengths followed the trend HT1>HT3>HT2 whereas the ductility followed HT3>HT2>HT1.
- HT3 offered a better combination of strength and ductility.

Acknowledgement

This study is partially supported by the National Aeronautics and Space Administration (NASA) under Cooperative Agreement No. 80MSFC19C0010 and the U.S. Department of Energy, Office of Science, Office of Basic Energy Sciences, under Award Number DE-SC0019378. This paper describes objective technical results

and analysis. Any subjective views or opinions that might be expressed in the paper do not necessarily represent the views of the NASA or the United States Government.

References

[1] Sjöberg G, Imamovic D, Gabel J, Caballero O, Brooks JW, Ferté J-P, et al. EVALUATION OF THE IN 939 ALLOY FOR LARGE AIRCRAFT ENGINE STRUCTURES 2004.

[2] EOS. Material Data Sheet EOS NickelAlloy IN939 Excellent High Temperature Performance with Corrosion Resistance n.d.

[3] Marchese G, Parizia S, Saboori A, Manfredi D, Lombardi M, Fino P, et al. The influence of the process parameters on the densification and microstructure development of laser powder bed fused inconel 939. Metals (Basel) 2020;10:1–19. https://doi.org/10.3390/met10070882.

[4] Shamsaei N, Yadollahi A, Bian L, Thompson SM. An overview of Direct Laser Deposition for additive manufacturing; Part II: Mechanical behavior, process parameter optimization and control. Addit Manuf 2015;8:12–35. https://doi.org/10.1016/j.addma.2015.07.002.

[5] Nandi I, Ahmad N, Shamsaei N, Shao S. Revealing texture induced abnormal tensile deformation behavior in additively manufactured Haynes 282 using crystal plasticity simulations n.d.

[6] Poudel A, Yasin MS, Ye J, Liu J, Vinel A, Shao S, et al. Feature-based volumetric defect classification in metal additive manufacturing. Nature Communications 2022 13:1 2022;13:1–12. https://doi.org/10.1038/s41467-022-34122-x.

[7] Shaikh AS, Rashidi M, Minet-Lallemand K, Hryha E. On as-built microstructure and necessity of solution treatment in additively manufactured Inconel 939. Powder Metallurgy 2023;66:3–11. https://doi.org/10.1080/00325899.2022.2041787.

[8] Jägle EA, Sheng Z, Wu L, Lu L, Risse J, Weisheit A, et al. Precipitation Reactions in Age-Hardenable Alloys During Laser Additive Manufacturing. JOM 2016;68:943–9. https://doi.org/10.1007/S11837-015-1764-2/FIGURES/5.

[9] Ghiaasiaan R, Ahmad N, Gradl PR, Shao S, Shamsaei N. Additively manufactured Haynes 282: effect of unimodal vs. bimodal γ′- microstructure on mechanical properties. Materials Science and Engineering: A 2022;831:142234. https://doi.org/10.1016/J.MSEA.2021.142234.

[10] Mišković Z, Jovanović M, Gligić M, Lukić B. Microstructural investigation of IN 939 superalloy. Vacuum 1992;43:709–11. https://doi.org/10.1016/0042-207X(92)90115-D.

[11] Banoth S, Li CW, Hiratsuka Y, Kakehi K. The Effect of Recrystallization on Creep Properties of Alloy IN939 Fabricated by Selective Laser Melting Process. Metals 2020, Vol 10, Page 1016 2020;10:1016. https://doi.org/10.3390/MET10081016.

[12] Shaw SWK. RESPONSE OF IN-939 TO PROCESS VARIATIONS n.d.

[13] Kanagarajah P, Brenne F, Niendorf T, Maier HJ. Inconel 939 processed by selective laser melting: Effect of microstructure and temperature on the mechanical properties under static and cyclic loading. Materials Science and Engineering A 2013;588:188–95. https://doi.org/10.1016/j.msea.2013.09.025.

[14] DOGU MN, Ozer S, Yalçın MA, Davut K, Bilgin GM, Obeidi MA, et al. Effect of Solution Heat Treatment on the Microstructure and Crystallographic Texture of In939 Fabricated by Powder Bed Fusion-Laser Beam. SSRN Electronic Journal 2023. https://doi.org/10.2139/ssrn.4365807.

[15] Šulák I, Babinský T, Chlupová A, Milovanović A, Náhlík L. Effect of building direction and heat treatment on mechanical properties of Inconel 939 prepared by additive manufacturing. Journal of Mechanical Science and Technology 2022;37:1071–6. https://doi.org/10.1007/s12206-022-2101-7.

[16] Formenti, A, Eliasson, A, Mitchell, A, Fredriksson, H. Solidification Sequence and Carbide Precipitation in Ni-Base Superalloys In718, In625 and In939. High Temperature Materials and Processes 2005;24:239–58. https://doi.org/10.1515/HTMP.2005.24.4.239.

[17] Tang YT, Ghoussoub JN, Panwisawas C, Collins DM, Amirkhanlou S, Clark JWG, et al. The Effect of Heat Treatment on Tensile Yielding Response of the New Superalloy ABD-900AM for Additive Manufacturing. In: Tin S, Hardy M, Clews J, Cormier J, Feng Q, Marcin J, et al., editors. Superalloys 2020, Cham: Springer International Publishing; 2020, p. 1055–65.

[18] Arhami F, Mirsalehi SE. The effect of heat treatment sequence on microstructure and mechanical properties of diffusion brazed IN-939 superalloy. J Mater Process Technol 2019;266:351–62. https://doi.org/10.1016/J.JMATPROTEC.2018.11.020.

[19] Muhammad M, Gusain R, Ghiaasiaan SR, Gradl PR, Shao S, Shamsaei N. Microstructure and Mechanical Properties of Additively Manufactured Haynes 230: A Comparative Study of L-PBF vs. LP-DED 2022. https://doi.org/10.26153/TSW/44174.

[20] Zhang Z, Chen DL. Consideration of Orowan strengthening effect in particulate-reinforced metal matrix nanocomposites: A model for predicting their yield strength. Scr Mater 2006;54:1321–6. https://doi.org/10.1016/J.SCRIPTAMAT.2005.12.017.